Density Fluctuations in Fluidized Beds

P. K. BAUMGARTEN and R. L. PIGFORD

University of Delaware, Newark, Delaware

The effectiveness of fluidized beds is limited by the presence of density fluctuations such as those caused by gas bubbles. The size and frequency of such bubbles were measured in air-fluidized beds of glass beads and silica-alumina catalyst with a gamma-ray absorption technique used.

The results showed that the gas bubbles developed owing to an influx of gas from the continuous dense phase. With increasing elevation in the bed the volumetric rate of bubble flow approached as a limit the total air flow minus the flow through the dense phase corresponding to minimum fluidization. The growth rate of bubble diameter was as much as 0.17 in./in. of elevation. Fluidization was most uniform with the cracking catalyst, for which the apparent density of the dense phase decreased with increasing gas velocity.

Gas-fluidized beds of fine particles are characterized by the presence of density fluctuations. Gas bubbles or pockets appear and result in an effective bypassing of the bed. The gas bubbles form spontaneously and grow in size as they rise through the bed. This action is evident to the eye and is an important factor in the performance of the bed in terms of mass transfer, heat transfer, or chemical reaction accomplished.

For instance measuring gas composition in a commercial cracking catalyst regenerator, Askins *et al.* (*1*) noted incomplete utilization of the regenerating air because a large fraction of the gas flow took place in bubble form. Wamsley Johanson (*18*) concluded that the nonuniformity impaired gas-solid heat transfer. Excessive pressure drop and fluctuations in pressure drop have also been attributed to the density fluctuations (*16, 15*).

Direct measurement of density fluctuations have been carried out in two cases. Morse and Ballou (*12*) measured local density variations with a capacitance probe, and Grohse (*5*) measured line-average densities by X-ray absorption. In both investigations it was observed that the density fluctuations became more pronounced with increasing gas velocity and at greater heights in the bed. Data obtained by Morse and Ballou also indicated that good initial gas distribution and increased bed height improved bed uniformity at lower levels. Conclusions regarding bypassing were chiefly qualitative, as no attempt was made in either study to determine gas bubble sizes or volumetric bubble flow rates.

Because of the recognized importance of this information to any attempts to compare efficiencies of fixed and fluid bed reactions, the chief objective of the present investigation was to measure the size and frequency of the gas bubbles appearing in fluidized beds and to compute the extent of gas bypassing from the data. It was also planned to investigate the relationships between appearance of bubbles, density gradients, and pressure drop through the bed. As suggested by different authors (*9, 16*) the fluidized bed consists of two phases: the continuous or dense phase composed of a more or less uniform mixture of solid particles and interstitial gas, and the discontinuous or bubble phase consisting of gas bubbles that are essentially free of solids. One aim of the present study was to determine the density of the dense phase and to study its relationship to the uniformity of density of the whole bed.

The experimental approach to the problem consisted of measuring continuously the fluctuating absorption of a horizontal gamma-ray beam that was directed through the bed from an external source. As the extent of absorption varied with the concentration of solid material in the path of the beam in accordance with the Lambert-Beer law, a detector placed opposite the source on the other side of the bed gave a continuous record of the fluctuating density within the bed. The similar technique employed by Grohse (5) was published after the present investigation had begun, but the published information (*5*) did not permit a detailed interpretation to be made of the magnitude of the fluctuations themselves.

This study was concentrated on the fluidization of spherical glass beads and silica-alumina cracking catalyst with air under atmospheric pressure used. Independent variables investigated included gas superficial velocity, particle size and size distribution, and bed height. Density measurements were made at different elevations in the bed, at different displacements from the center line of the bed, and along two horizontal paths of different length.

EXPERIMENTAL

Apparatus

The fluidization and gamma-ray apparatus is shown diagrammatically in Figure 1, and the fluidization column is shown with the gamma-ray source and detector in Figure. 2. Figure 3 shows the arrangement used for calibration. Fluidization was carried out in a 3- × 6-in. rectangular column of transparent acrylic resin. Filtered and dried air entered the column through a packed section and a 3/32 in. thick sintered bronze distributor plate (pressure drop 0.8 in. of water at 2 ft./sec. superficial air velocity). Entrained solids were separated in a disengaging zone of large cross section situated above tthe column. Pressure taps equipped with filters were located just below the distributor plate and at different levels above it. Pressures were read on water *U*-tube manometers damped by constricting the base of the *U*. The gamma-ray apparatus consisted of the source and source holder, a collimator to form the gamma-ray beam, one or more attenuators to reduce beam intensity, and instruments to detect the transmitted radiation, record its mean intensity, and measure the size of its fluctuations.

Preliminary experiments with a 100-millicurie source of cerium 144-praseodymium 144 demonstrated the importance of providing a gamma-ray beam of the right intensity and penetration for a given bed of solids. Best results were obtained when the fraction of incident radiation transmitted by the bed was between 0.05 and 0.50. The final absorption measurements were carried out with a 200-mg. source of thulium 170. This source (*17*) provided a high intensity gamma-ray beam of relatively low penetrating power, required to minimize the effect of source noise resulting from the random nature of radioactive decay (*13*). Ordinarily source noise can be reduced by lengthening the period of observation, but in this case the need to observe frequent density fluctuations made this impossible. Reduction of source noise permitted detection of air bubbles having a diameter as small as 0.35 in. in the case of the glass beads or about 0.7 in. in the case of the cracking catalyst, as calculated from statically determined noise levels and absorption coefficients. The difference in the two cases was due to the larger absorption coefficient of the glass beads.

The shielded source holder could be

P. K. Baumgarten is with E. I. du Pont de Nemours and Company, Wilmington, Delaware.

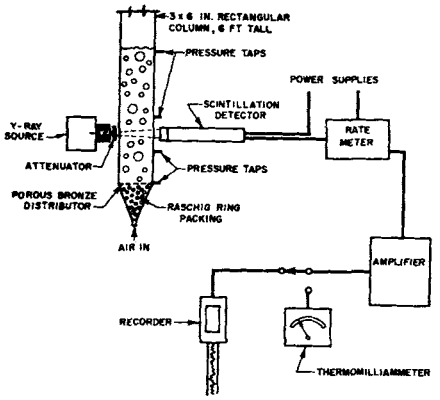

Fig. 1. Schematic diagram of apparatus.

freely positioned to irradiate different portions of the fluidized bed. By proper placement of the source the fine gamma-ray beam, a 3.2 deg. cone, was made to have the same average diameter of 0.44 in. within the fluidized bed for both the 3- and 6-in. paths.

Instruments for detecting tthe transmitted radiation and for indicating and recording the resulting signal were chosen for their rapid response to changes in the level of the transmitted radiation. This radiation, usually in the range of 10,000 to 60,000 counts/sec., was sensed by a scintillation detector and converted to electrical pulses. A pulse-rate meter employing an especially designed circuit emitted a voltage that depended on the pulse rate. The rate-meter output was passed on to a direct-writing oscillograph for continuously recording the bed's apparent density. A thermomilliammeter was also provided to measure the root-mean-square voltage of the rate-meter output. Calibration in terms of bed density permitted conversion of the thermomilliammeter reading to the standard deviation of the densiy fluctuations. To minimize detection of scattered radiation the scintillation detector intercepted the major portion of the gamma-ray beam and was positioned at a sufficient distance from the fluidization column. The rate meter gave approximately logarithmic response so that its output was an approximately linear function of fluidized-bed density.

The instruments were periodically calibrated with different thicknesses of the powdered material under study used. As shown in Figure 3 the material used for calibration was contained in *U*-shaped brass cells, the front and back of which consisted of tightly stretched paper, giving negligible absorption. Calibration compensated for a number of factors difficult to assess oherwise, such as source decay, unequal absorption of different portions of the gamma-ray spectrum, scattered radiation, and rate-meter coincidence loss.

Materials

Table 1 lists the physical properties of the materials used: commercial spent silica-alumina cracking catalyst and four grades of spherical glass beads. Three grades of the glass beads were relatively narrow size fractions. The fourth grade was a blend prepared by mixing the largest and smallest size narrow fractions in proportion, so that the mean particle diameter would be the same as for the intermediate size narrow fraction. The mean particle diameters given are the volume-surface means (7). The particle density was determined by displacement in methyl alcohol and represents the skeletal density. The settled bed density was the density of the bed that had settled from a vigorously fluidized state after the flow of air was suddenly stopped and no external means were used to compact the bed. The minimum fluidizing velocity was determined as described later. Under the microscope the glass beads appeared almost spherical, while the cracking catalyst particles were rounded and oblong in shape like pebbles.

Procedure

The column was charged with the powder, and pressure drop and the depth of the bed were observed with both increasing and decreasing gas velocity from below the minimum fluidizing velocity to about 2 ft./sec., the highest air velocity employed. The source and detector were then put in position. Instantaneous and time-average oscillographs, with integrator time constants of 0.015 and 5.25 sec. used, respectively, were obtained. The thermomilliammeter reading was obtained, usually an average of ten random readings to even out the meter fluctuations. The calibration curve for the powder and the particular attenuation was secured either before or after the fluidization runs. The absorption by the settled bed was also determined.

ANALYSIS OF GAMMA-RAY DATA

The original oscillograms and thermomilliammeter readings required suitable interpretation to obtain values for bubble size, bubble frequency, and bubble velocity. Figure 4 shows typical strip-chart oscillograms. The two instantaneous oscillograms taken at different speeds, both with an integrator time constant of 0.015 sec., indicate the time dependence of line-average density of the fluidized bed along the path of the gamma-ray beam. The trace obtained with the long-time constant of 5.25 sec. gives the time-average density. In the instantaneous oscillograms the small fluctuations near the top of the trace represent the background noise at an average level equivalent to the density of the dense phase. The large pulses extending below the dense-phase density result from the passage of bubbles through the gamma-ray beam. The distance of the peaks below the dense-phase density corresponds to the maximum thickness of the bubble as sensed by the gamma-ray detector.

Also indicated on the charts are the calibration of the oscillograms in terms of the specific gravity of the bed relative to the settled bed and the number of trace pulses counted as bubbles. The standard deviation of the instantaneous oscillogram, including the source noise, is given by the thermomilliammeter reading σ_m. Fluctuations in the oscillograms of the same order of magnitude as the source noise were omitted in the bubble count, with statistical criteria used as a guide. Specifically oscillogram fluctuations extending less than three times the standard deviation of the noise below the dense-phase density were excluded. Also, adjoining bubble traces were counted separately only if they extended more than $3\sqrt{2}\sigma_N$ beyond the trough between them.

The treatment of the experimental data consisted of calculation of a mean apparent bubble thickness from the thermomilliammeter reading and the mean bed density, conversion of this quantity to the mean bubble diameter, correction of observed bubble frequency to include bubbles outside the gamma-ray beam, and calculation of superficial and true bubble velocities. The first step could also have been accomplished by measuring individual bubble sizes on the strip charts, but this method proved

Table 1. Physical Properties of Materials

Mean particle diameter, D_p, μ	Particle-size range, μ	ρ_p, g./cc.	ρ_s, g./cc.	ϵ_s	ϵ_s	u_{omf}, ft./sec.
Glass beads, narrow fractions						
74	38-124*	2.44	1.40	0.427	0.429	0.024
119	61-175*	2.45	1.42	0.421	0.426	0.054
234	147-495*	2.60	1.56	0.400	0.404	0.17
Blend of glass beads (45.1 wt.% of $D_p = 74\mu$ and 54.9 wt.% of $D_p = 234\mu$)						
116	38-495*	2.52**	1.60	0.365	0.379	0.035
Silica-alumina cracking catalyst						
41	0-120†	2.17	0.813	0.628	0.628	0.024

* Determined by screen analysis.
** Calculated from the properties of the two components.
† Determined by Roller analysis.

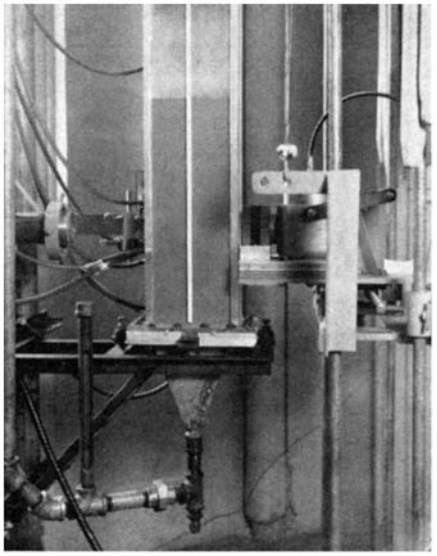

Fig. 2. Source and detector with fluidized bed.

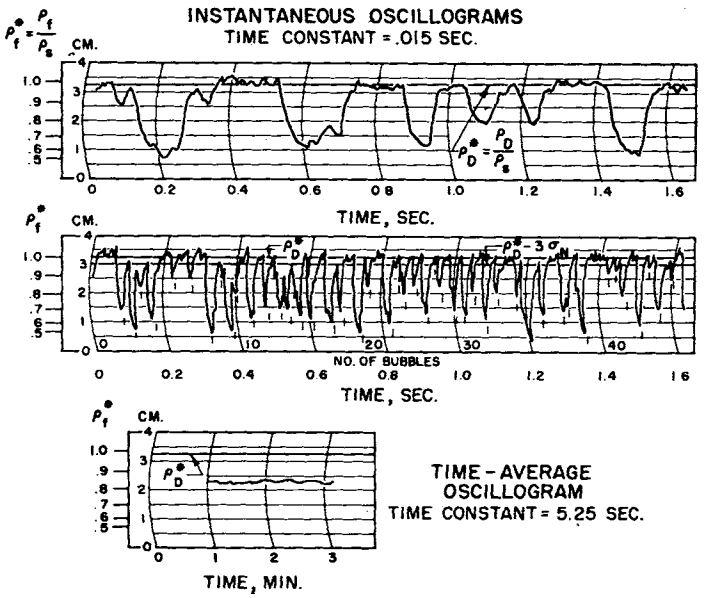

Fig. 4. Typical strip-chart oscillograms; glass beads, $D_p = 119\ \mu$; 6-in. path, $u_0 = 0.20$ ft./sec.; 15-in. settled-bed height, 8-in. level.

too time consuming for all but a few cases and the alternate statistical method described below was devised.

Mean Apparent Bubble Thickness

The calculation of the mean apparent bubble thickness will be illustrated by the idealized oscillogram depicted in Figure 5. $a(x, \theta)$ is defined as the concentration of dense phase or fraction of fluidized bed occupied by the dense phase at any point within the fluidized bed. According to its definition a can be either zero if x lies inside a bubble or one if x lies in the dense phase. Then along the beam the line-average concentration of dense phase at any time is

$$\bar{a}(\theta) = \frac{1}{X}\int_0^X a(x, \theta)\,dx \qquad (1)$$

As $\bar{a}$ is a function of time, the time-average of the line-average concentration of dense phase is given by

$$\langle\bar{a}\rangle = \operatorname{Lim}_{T\to\infty}\frac{1}{T}\int_0^T \bar{a}(\theta)\,d\theta \qquad (2)$$

and the variance of the line-average concentration by

$$\sigma_{\bar{a}}^2 = \operatorname{Lim}_{T\to\infty}\frac{1}{T}\int_0^T (\bar{a} - \langle\bar{a}\rangle)^2 d\theta$$

$$= \operatorname{Lim}_{T\to\infty}\left[\frac{1}{T}\int_0^T \bar{a}^2\,d\theta\right] - \langle\bar{a}\rangle^2 \qquad (3)$$

The value of $\langle\bar{a}\rangle$ was obtained from the oscillograms by the equation

$$\langle\bar{a}\rangle = \frac{\rho_f^*}{\rho_D^*} \qquad (4)$$

The value of $\sigma_{\bar{a}}^2$ was obtained from the thermomilliammeter reading σ_m in terms of settled-bed density by allowing for the density of the dense phase, by the use of

$$\sigma_{\bar{a}}^2 = \left(\frac{1}{\rho_D^*}\right)^2 \sigma_{\rho_f^*}^2$$

$$= \frac{1}{\rho_D^*}\left[\sigma_m^2 - \sigma_N^2\right] \qquad (5)$$

Subtraction of the variance of the source noise σ_N^2 corrected for the small increase in the observed variance caused by random emission. In the few cases where σ_N^2 was a substantial fraction of σ_m^2, the mean apparent bubble thickness was determined from the strip charts.

The mean apparent bubble thickness was calculated from $\langle\bar{a}\rangle$ and $\sigma_{\bar{a}}^2$ by assuming that the passage of individual bubbles through the beam could be represented by separate rectangular deflections on the oscillogram, all of which were uniform in size. As shown by Figure 5 each bubble trace was assumed to have duration δ and height x_b/X, so that the value of $\bar{a}(\theta)$ during the passage of the bubble was $(X - x_b)/X$. In the absence of bubbles from the beam the radiation intensity reverted to that cor-

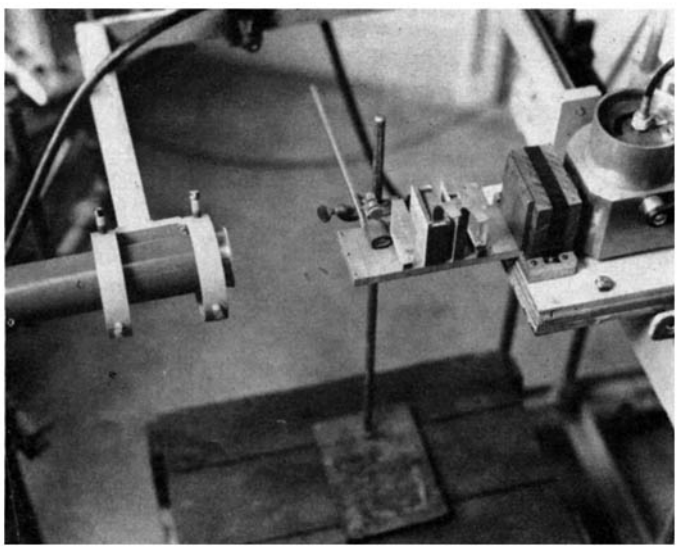

Fig. 3. Source and detector during calibration.

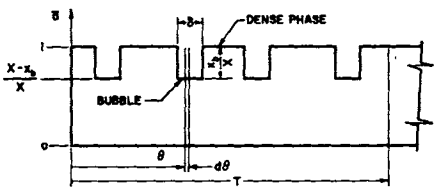

Fig. 5. Idealized strip-chart oscillogram.

responding to the dense-phase density, with $\bar{a} = 1$. Bubble traces occurred at random intervals, with a frequency f_b.

Equations (2) and (3) for $<\bar{a}>$ and $\sigma_{\bar{a}}^2$ were applied to the idealized oscillograms to yield expressions in terms of f_b, δ, and x_b. The results were combined and solved for x_b and

$$<\bar{a}> = \lim_{T\to\infty} \frac{1}{T}\left\{\left[\int_0^T \bar{a}\, d\theta \right.\right.$$

$$\left. \text{for the dense phase} \right]$$

$$+ \left[\int_0^T \bar{a}^2\, d\theta \text{ for bubbles}\right]\Big\}$$

$$= \lim_{T\to\infty} \frac{1}{T}\left\{[1\cdot(T - Tf_b\,\delta)]\right.$$

$$\left. + \left[\frac{X - x_b}{X}(Tf_b\,\delta)\right]\right\}$$

$$= 1 - f_b\,\delta(x_b/X) \qquad (6)$$

$$\sigma_{\bar{a}}^2 = \lim_{T\to\infty} \frac{1}{T}\left\{\left[\int_0^T \bar{a}^2 d\theta \right.\right.$$

$$\left. \text{for the dense phase} \right]$$

$$+ \left[\int_0^T \bar{a}^2\, d\theta \text{ for bubbles}\right]\Big\}$$

$$- <\bar{a}>^2$$

$$= \lim_{T\to\infty} \frac{1}{T}\left\{[1\cdot(T - Tf_b\,\delta)]\right.$$

$$\left. + \left[\left(\frac{X - x_b}{X}\right)^2 Tf_b\,\delta\right]\right\}$$

$$- <\bar{a}>^2$$

$$= \left(\frac{x_b}{X}\right)^2 [f_b\,\delta - f_b^2\,\delta^2] \qquad (7)$$

Solving Equations (6) and (7) simultaneously one gets

$$x_b = X\left[1 - <\bar{a}> + \frac{\sigma_{\bar{a}}^2}{1 - <\bar{a}>}\right] \qquad (8)$$

and

$$\delta = \frac{1 - <\bar{a}>}{(x_b/X)f_b}$$

Since all bubble traces were assumed to be of the same size, $\bar{x}_b = x_b$.

In spite of the drastic assumptions employed in this derivation values of $\bar{x}_b$ calculated by Equation (8) with the use of $\sigma_{\bar{a}}^2$ from the thermomilliammeter were found to agree substantially with means of values obtained from the strip charts by measuring individual pen deflections beyond the background noise. The remarkable agreement is seen in Figure 6, where values of

$$X\left[1 - <\bar{a}> + \frac{\sigma_{\bar{a}}^2}{1 - <\bar{a}>}\right]$$

are plotted against strip-chart values of $\bar{x}_b$ for eleven different runs. No improvement in these results was obtained by modifying Equations (6) and (7) to allow for the varying shapes of the bubble traces. $\bar{x}_b$ was therefore calculated by Equation (8) in most cases.

It might be thought that the diameter of the gamma-ray beam had an effect on the value of mean bubble thickness. It was found experimentally however that reducing the diameter of the beam by one half had no appreciable effect on the values of $\bar{x}_b$ obtained.

Bubble Diameter

When a bubble passed through the gamma-ray beam, transmission of gamma radiation was largest at the instant the bubble center was at the same horizontal level as the beam's axis. At this instant however the bubble center may have been some horizontal distance y away from the beam axis. On the assumption that the bubbles were spheres and that all values of y within the bounds set by the column walls were equally probable, the bubble's diameter was obtained from the mean apparent bubble thickness as follows:

$$\bar{x}_b = \frac{\int_0^{D_b/2} x_b\, dy}{\int_0^{D_b/2} dy}$$

$$= \frac{2\int_0^{D_b/2} \sqrt{(D_b/2)^2 - y^2}\, dy}{D_b/2}$$

$$= \frac{\pi}{4} D_b \qquad (10)$$

Hence

$$D_b = \frac{4}{\pi}\bar{x}_b \qquad (11)$$

This relationship was used except in the few cases where Equation (11) indicated a value of D_b larger than the width of the bed; then the bed dimension itself was used as D_b.

Bubble Frequency

To obtain the value of the bubble frequency for the entire bed cross section it was necessary in some cases to apply a correction factor to the bubble frequency read from the oscillograms. The correction factor allowed for the fact that not all bubbles passed through

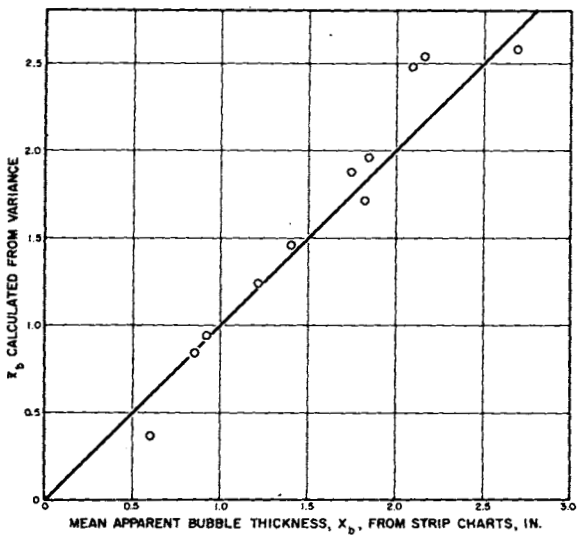

Fig. 6. Comparison of bubble thicknesses from variance and oscillogram.

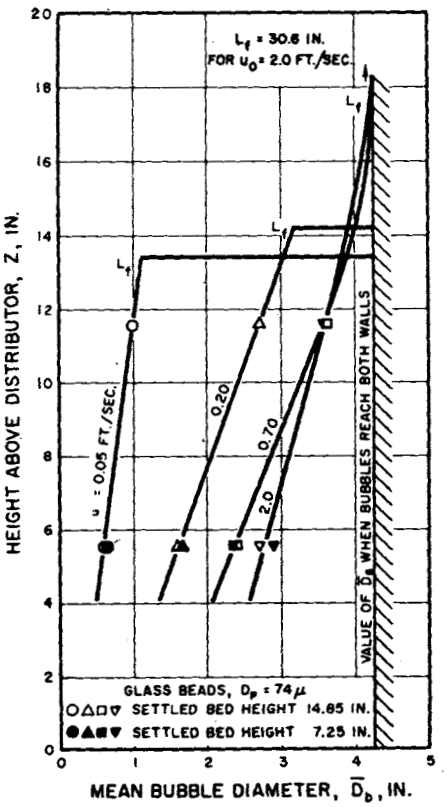

Fig. 7. Vertical bubble-size profiles.

the gamma-ray beam. It was assumed that the gamma-ray instruments probed a bed width equal to the sum of the beam diameter and twice the average bubble diameter in the direction across the gamma-ray beam. For the 6-in. path the corrected frequency was

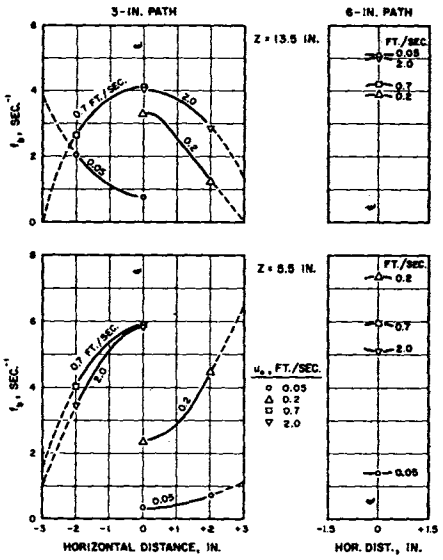

Fig. 8. Horizontal bubble-frequency profiles; glass beads, $D_p = 74\ \mu$, 15-in. bed.

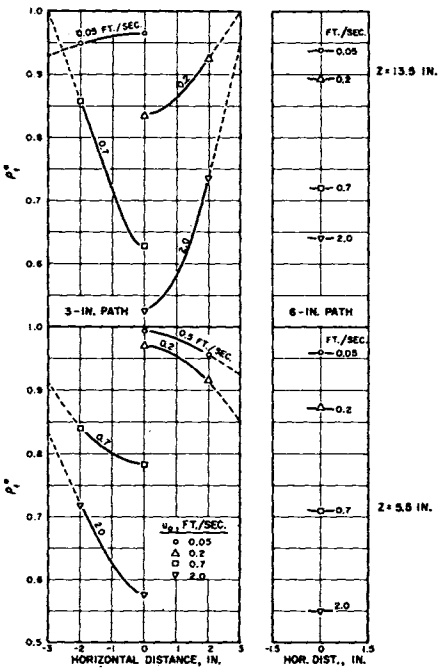

Fig. 9. Horizontal density profiles; glass beads, $D_p = 74\ \mu$, 15-in. bed.

$$f_b' = \frac{3}{2(D_b)_{3\text{-in.}} + D_\gamma} (f_b)_{6\text{-in.}} \qquad (12)$$

Here $(D_b)_{3\text{-in.}}$ is the average bubble diameter measured along the 3-in. path, and $(f_b)_{6\text{-in.}}$ is the observed bubble frequency measured along the 6-in. path and read on the strip-chart oscillogram. As a rule the bubble frequency for the 6-in. path was employed for the calculation of f_b' because the factor correcting f_b was usually smaller for the 6-in. path than for the 3-in. path and could often be omitted.

Bubble Velocity

The volumetric flow of the gas in the form of bubbles equals the product of the mean bubble volume and the frequency of bubbles at the given bed level. It was assumed that the average bubble volume was the same as that of an ellipsoid having horizontal axes equal to the experimentally observed bubble diameters along the 3- and 6-in. paths and having a vertical axis equal to the geometric mean of the two diameters. This assumption could be made for superficial gas velocities of 0.7 ft./sec. or less, since in these cases the visually observed bubbles were about the same size horizontally and vertically. The superficial bubble velocity was obtained by dividing the volumetric bubble flow by the column cross section giving

$$u_{B0} = \frac{1}{S} \cdot \frac{\pi}{6} (D_b)_{3\text{-in.}}^{1.5} (D_b)_{6\text{-in.}}^{1.5} f_b' \qquad (13)$$

Values of u_{B0} were not calculated for gas velocities greater than 0.7 ft./sec., since there was no way of estimating the vertical elongation of the bubbles. Since the source noise associated with the gamma-ray measurements set a lower limit to the size of the bubbles detected, Equation (13) and all other equations involving u_{B0} should be understood to include only bubbles larger than the minimum size detectable.

If $\langle \bar{a} \rangle$ is close to the average fraction of the bed occupied by the dense phase at any given level, the true bubble velocity is

$$u_b = \frac{u_{B0}}{1 - \langle \bar{a} \rangle} \qquad (14)$$

The superficial velocity of the gas through the dense phase was obtained by

$$u_{D0} = u_0 - u_{B0} \qquad (15)$$

Combining Equations (14) and (15) one obtains

$$u_{D0} = u_0 - u_b (1 - \langle \bar{a} \rangle) \qquad (16)$$

This equation shows that if $\langle \bar{a} \rangle$ is the same at all heights above the distributor, then the portion of gas passing through the dense phase will decrease with increasing true bubble velocity.

Reproducibility

The precision of the results was determined by making frequent duplicate determinations. The standard deviations of error for single determinations were 0.018 for ρ_f^*, 0.24 in. for $\overline{D}_b$, and 0.29 sec.$^{-1}$ for f_b. Representative standard deviations for u_{B0} and u_b were from 30 to 50%, as calculated with well-known principles of the propagation of independent errors (*14*) used. Most of the data presented herein have about half this variability because of the duplicate determinations.

The reproducibility obtained was good, considering that conditions in the fluidized bed changed constantly owing to the nature of the bed itself. Measurements over much longer time periods would have been necessary to improve reproducibility to any large extent.

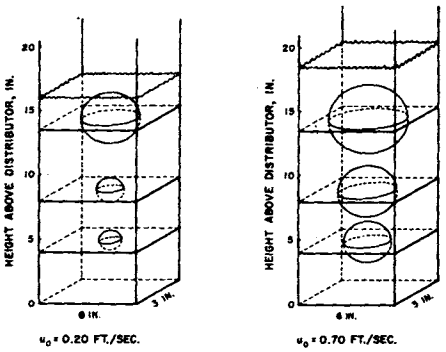

Fig. 10. Horizontal dimensions of bubbles; blend of glass beads.

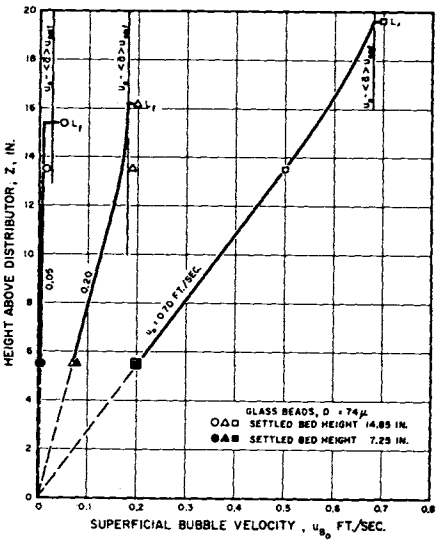

Fig. 11. Bubble flow rate as function of height above distributor.

RESULTS AND DISCUSSION

Bubble Size, Frequency, and Density

Observed values of mean bubble diameter, bubble frequency, and horizontal density are shown for a 15-in. bed of 74-μ glass beads in Figures 7, 8, and 9, respectively. The estimated cross sections of an average bubble at different elevations in the bed are shown for

the blend of glass beads in Figure 10. Results are presented in detail elsewhere (3).

The fast growth of the rising bubbles from the initially small size is apparent from Figures 7 and 10. Bubbles are seen to grow until they approach or even reach the walls of the column. Then as a result of wall effects they become elongated in the direction of the longer dimension of the rectangular column. Bubble size is very evidently affected by superficial air velocity increasing with increasing u_0.

Bubble frequencies measured at different locations in the bed and along the 3- and 6-in. paths ranged from 0.3 to 7.3/sec., as shown by Figure 8. When the bubbles were large, the bubble frequency was highest at center of the column. A large bubble cross section forced the bubbles away from the walls. Small bubbles were found somewhat more frequently near the wall than along the axis, growth of large bubbles by coalescence apparently being easier away from the walls. Bubble frequencies measured along the 6-in. path were usually greater than along the 3-in. path, as would be expected if about the same number of bubbles occurred in any given path length. In cases where bubbles were large, bubble frequencies for the 3- and 6-in. paths were about the same, indicating that only a single bubble could occur in the available bed cross section in a given time interval.

The combined effects of bubble size and frequency resulted in nonuniform horizontal profiles of mean relative density, as shown by Figure 9. The mean density ranged from 55 to 99% of the settled bed density, depending on air velocity and location in the bed. As might be expected the density of the bed was found to be low where bubbles were frequent and large. Except when beds were very turbulent, the average bed density calculated from the observed height of the bed came within a few percentages of the densities determined by gamma-ray absorption. In some cases where bubbles were large, the time-average density measured along the 6-in. path was less than along the 3-in. path. In those cases it must be presumed that the greater wall interference along the 3-in. bed dimension prevented the bubbles from assuming random positions in that direction. Therefore the maximum bubble dimension, and the lowest bed density, tended to concentrate along the center 6-in. path.

Data were also obtained for a shallower bed of 74-μ glass beads, 7.5 in. tall. Results almost duplicated data for the 15-in. bed taken at the same bed level, as seen in Figure 7 for the case of average bubble diameter. Similar good agreement was also found for bubble frequency and bed density. These data indicate that the depth of the bed did not affect its uniformity at a given level. Uniformity therefore appears to be independent of the mass of fluidized material that may be present above the level in question.

Although no direct observations were made of solids circulation patterns, the results on bubble size, frequency, and bed density give indications of what these patterns may have been. When bubbles were small and well distributed over the cross section of the bed, the solid particles must have been pushed aside by the bubbles or possibly lifted a short distance until the bubble passed. When bubbles were large however and rose in the center of the fluidized bed, the solid particles would have been raised by the bubbles in the center of the bed for a considerable distance and then would have moved downward near the walls. Thus an increase in the air velocity would be expected to change the circulation pattern of the dense phase from small, localized motion to increasingly larger patterns extending throughout the beds.

Pressure Drop through the Bed and Vertical Density Profiles

In the past, variation of the pressure drop through the fluidized bed and of the rate of bed expansion with increasing gas velocity has been used to characterize fluidization quality. Gamma-ray determination of line-average densities now permits closer examination of the meaning of such information. If the friction experienced by the gas as it flows through the interstices of the bed is just sufficient to support the weight of all the particles in the bed, the vertical pressure gradient will be proportional to the density of the bed, as in the case of a liquid. The relationship between pressure gradient and bed density is then expressed by the hydrostatic equation

$$\frac{dp}{dZ} = -\frac{g_L}{g_c}\rho_f \qquad (17)$$

Integration gives

$$p_{z_1} = \frac{g_L}{g_c}\int_{z_1}^{L_f} \rho_f(Z)\,dZ \qquad (18)$$

for the pressure at a distance of Z_1 above the distributor plate. For $Z_1 = 0$, and in terms of water manometer readings, H, and bed density relative to settled bed this equation becomes

$$H = \frac{\rho_S}{\rho_W}\int_0^{L_f} \rho_f^*\,dZ \qquad (19)$$

where ρ_S/ρ_W is the specific gravity of the settled bed relative to water, the gauge fluid. When one assumes a uniform bed, the value of H also should be given by

$$H = \frac{1}{\rho_W}\frac{g_c}{g_L}\left(\frac{W}{S}\right) \qquad (20)$$

Table 2 shows a comparison of values of H obtained from manometer readings, calculated from vertical density profiles measured by gamma-ray absorption with Equation (19) used, and calculated from the weight of the powder with Equation (20) used. The value of L_f used in Equation (19) was the visually observed average height of the bed.

It will be noted that agreement between the pressure drops is good at the lowest air velocity but that it becomes increasingly poorer with increasing air velocity. Agreement among the gamma-ray data obtained along different paths also becomes poorer with increasing air velocity. It is thus seen that when the fluidized bed is not uniform, the analogy between fluidized bed behavior and hydrostatic behavior of a liquid no longer

Table 2. Prediction of Pressure Drop
Total pressure drop, in. Water, 15-in. bed of 74-μ glass beads

Superficial air velocity, ft./sec.	0.05	0.2	0.7	2.0
Observed manometer reading	20.8	20.5	20.8	22.0
Calculated from gamma-Ray measurements				
from density along 3-in. path, center	21.1	20.2	17.6	17.1
from density along 3-in. path, off center	20.4	20.3	21.3	23.5
from density along 6-in. path, center	20.6	19.2	17.5	19.2
Calculated from weight of powder	20.8	20.8	20.8	20.8

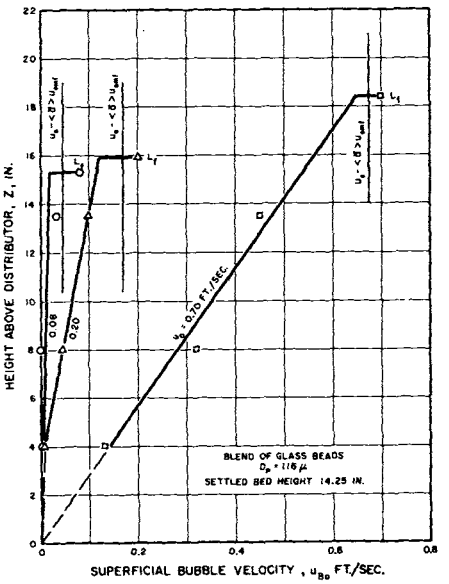

Fig. 12. Bubble flow rate as function of height above distributor.

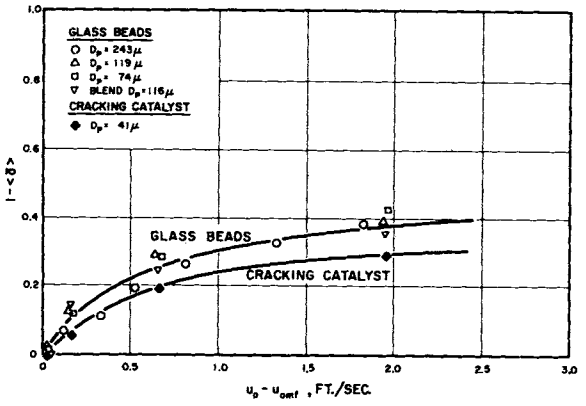

Fig. 13. Fraction of fluidized bed occupied by bubbles.

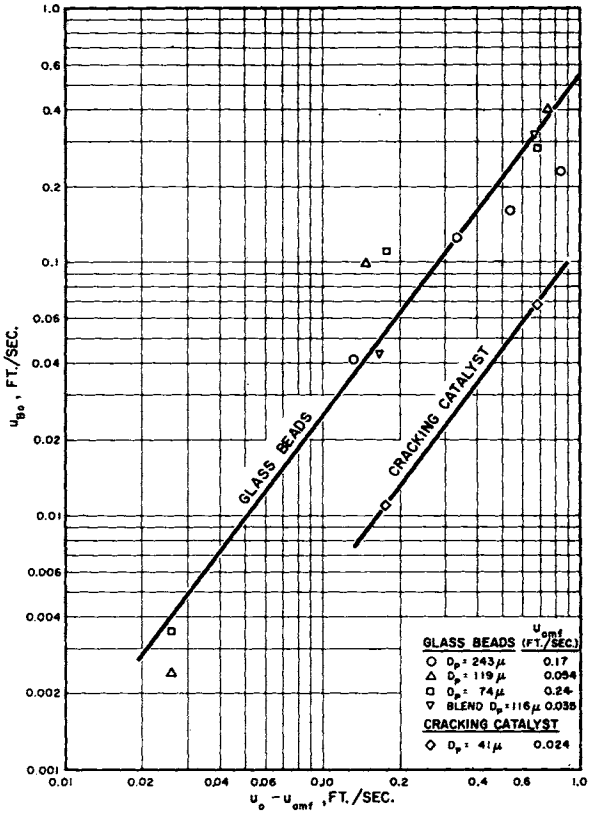

Fig. 14. Bubble flow rate—effect of air velocity.

holds. It can also be inferred that the slow increase of the manometer reading at air velocities from 0.2 to 2.0 ft./sec. results at least in part from the uneven horizontal distribution of the powder in the bed. Similar occurrence of excess pressure drop reported by some authors (*9, 16*) was probably also due in part to wall effects, that is to the accumulation of solid particles near the walls when large bubbles occupied the center of the column.

Bubble Flow Rate

The superficial bubble velocity was calculated from the gamma-ray data on bubble size and frequency with the calculation scheme as outlined earlier used. The value of u_{Bo} is in effect a measure of gas bypassing and is of real interest in the interpretation of gas-particle heat transfer and chemical reaction data obtained in fluidized beds. Figures 11 and 12 give values of u_{Bo} plotted against height above the distributor for two sizes of glass beads. Only total air velocities of 0.7 ft./sec. or less are included, because the calculation scheme does not apply if the bubbles are appreciably elongated in the vertical direction. The data show that the bubble flow rate in bubbles of detectable size increases almost linearly with increasing elevation in the bed. By detectable size is meant the bubble size that could be detected and identified by gamma-ray absorption. The minimum detectable bubble diameter was about 0.35 in. in the case of the glass beads. As indicated by the data the measured bubble flow rate has a value close to zero just above the distributor. As Z is increased, u_{Bo} approaches the quantity $u_o - <\bar{a}> u_{omf}$ indicated by the vertical straight lines. This quantity is the total gas flow minus the gas flow that would occur in the dense phase at the minimum fluidizing velocity, all based on the column cross section. When $u_{Bo} = u_o - <\bar{a}>\ u_{omf}$, the dense phase carries the quantity of gas corresponding to quiescent fluidization, as suggested by Toomey and Johnstone (*16*). It will be noted from the data however that this condition was reached only at an appreciable elevation above the distributor and did not occur in the bottom of the fluidized bed.

Although very small bubbles were not included in the measured value of u_{Bo}, the gas flow contained in them was probably quite small. Very many of these bubbles would have been necessary to carry the same quantity of gas as the large bubbles actually detected. The presence of such a large number would have had the effect of reducing the density of the dense phase. Such a reduction was not observed in the case of the glass beads. Hence the observed increase in bubble flow rate with increasing height above the distributor is believed to reflect at least qualitatively the actual situation.

As a result of this reasoning the following picture may be given of the formation of bubbles in fluidized beds. Just above the distributor the fluidized bed is a relatively uniform mixture of solid and gas. The gas velocity through the interstices of the bed is greater than the velocity needed to support the particles. Thus there is an excess of gas flowing in the dense phase. As the dense phase becomes unstable, the supporting gas flows into local regions of accidentally low density in the solid structure and forms embryo bubbles essentially free of solids. The gas encounters frictional resistance in flowing out of the dense phase. Hence there is a finite time of bubble formation. Once the bubbles are formed, they grow by coalescence with neighboring or slower rising bubbles and by sweeping up additional gas from the dense phase. Finally some distance above the distributor the gas flow through the dense phase becomes equal to u_{omf}, the quantity which is just needed to support the particles. Beyond this point bubbles grow only by coalescence.

The Minimum Fluidizing Velocity

As noted above the minimum fluidizing velocity is an important parameter needed for understanding fluidized-bed behavior. It marks the transition from a settled or quiescent bed, in which all of the gas flow takes place in the interstices between the particles, to a fully fluidized bed, in which the gas flow supports the weight of the solids and in which part of the gas flow may be in the form of bubbles. Although the transition is not necessarily sharp, the following relations may be assumed to hold for $u_o = u_{omf}$:

$$\begin{aligned} <\bar{a}> &= 1 \\ D_b &= 0 \\ u_{Bo} &= 0 \end{aligned} \qquad (21)$$

Values of the minimum fluidizing velocity were determined by the method of Miller and Logwinuk (*11*). They are listed in Table 1. These values agreed well with the air velocity at which

bubbles were first observed to break through the surface of the bed. They also agreed with values of u_{omf} obtained from the correlations of Baerg *et al.* (2), which were developed from heat transfer data. Values of the experimental minimum fluidizing velocity were correlated within 10% by

$$u_{omf} = \frac{\epsilon_s'^3 \phi_p^2 D_p^2 (\rho_p - \rho_f) g_L}{144(1 - \epsilon_s')\mu_f} \qquad (22)$$

Here ϵ_s' is observed after decreasing the air velocity slowly from the fluidization range. The equation is a combination of the well-known equation of Carman-Kozeny (4), applicabe to randomly packed fixed beds, with the condition that the pressure difference equals bed weight per unit cross section. The constant 144 in Equation (22) is empirical and only slightly different from the value 180 commonly employed in the packed-bed correlation. The equation represented the minimum fluidizing velocity both for the spent cracking catalyst and for the glass beads. Since the catalyst had probably lost most of its porosity compared with fresh catalyst, the skeletal density (given as ρ_p in Table 1) could be employed in Equation (22) without introducing appreciable error.

Effect of Air Velocity and of Particle Parameters

The volume fraction of the fluidized bed occupied by bubbles is shown in Figure 13 as a function of the superficial air velocity minus the minimum fluidizing velocity. The upper line is a plot of the equation

$$1 - \langle \bar{a} \rangle = 0.3(u_o - u_{omf})^{0.4} \qquad (23)$$

and represents the points for the glass beads. Points for the cracking catalyst fall on a separate line. Values of $\langle \bar{a} \rangle$ are those for the centered 6-in. path at the 8-in. level, which are believed to represent closely the average values of $\langle \bar{a} \rangle$ over the whole bed. The plot indicates that the chief factor affecting the concentration of bubbles in the bed is the gas flow. Subtraction of the minimum fluidizing velocity from the superficial gas velocity recognizes that bubbles do not appear until the bed is a minimum fluidization.

The superficial bubble velocity at the 8-in. level is similarly plotted against $u_o - u_{omf}$ in Figure 14 for total superficial gas velocities up to 0.7 ft./sec. Separate lines are again obtained for the glass beads and the cracking catalyst, with the glass beads giving the greater bubble flows. Although correlation of the glass-bead data is relatively good, some scatter is evident, showing that correction of u_o by subtracting u_{omf} does not compensate completely for different particle size or particle-size range. Comparison of the points for the blend and narrow fraction of the same particle size indicates less gas bypassing for the blend at $u_o - u_{omf} \sim 0.16$ ft./sec. but little or no difference at $u_o - u_{omf} \sim 0.66$ ft./sec. Hence no clear-cut advantage is indicated for using a wide rather than a narrow size fraction to reduce gas bypassing.

As shown by Figures 11 and 12 the bubble velocity reached the value $u_o - \langle \bar{a} \rangle u_{omf}$ at a sufficient elevation in the fluidized bed. For this reason the differences in u_{Bo} shown for different powders in Figure 14 are chiefly indications of different rates of bubble growth. The rate of bubble growth is shown to be a function of particle size and other particle parameters; it is very noticeably smaller for the cracking catalyst than for the glass beads.

Density of the Dense Phase

In spite of the turbulent motions existing in a vigorously fluidized bed it was interesting to note that the density of the dense phase of the glass beads did not differ greatly from that of the settled bed. Table 3 presents the observed specific gravity of the dense phase for the different materials and different air velocities. For the glass beads the dense-phase density was always within 2% of the settled-bed density with the single exception of the blend of glass beads at $u_o = 0.08$ ft./sec., where the difference was still only 8%.

Widely different results were obtained for the silica-alumina cracking catalyst however. For this material the dense phase expanded to a density only 60% of the settled-bed density. Only part of this indicated expansion may have been a uniform expansion of the dense phase, the rest being due to the appearance of many small bubbles not detectable by gamma-ray absorption. The minimum detectable bubble size for the cracking catalyst was about twice that for the glass beads. Hence an appreciable portion of the bubble flow through this material could have been in the form of small bubbles. It is therefore possible that the actual volumetric bubble flow for the cracking catalyst was just as large as for the glass beads. The average bubble size however was much smaller for the cracking catalyst. This would be advantageous from the standpoint of achieving good gas-solids contact, since gas interchange between bubbles and dense phase would occur more readily through the greater bubble surface.

It is interesting to speculate whether a blend of glass beads could be prepared which would fluidize as uniformly as the cracking catalyst, that is whose dense phase would undergo large expansion and whose measured bubble flow rate would be as small. The data

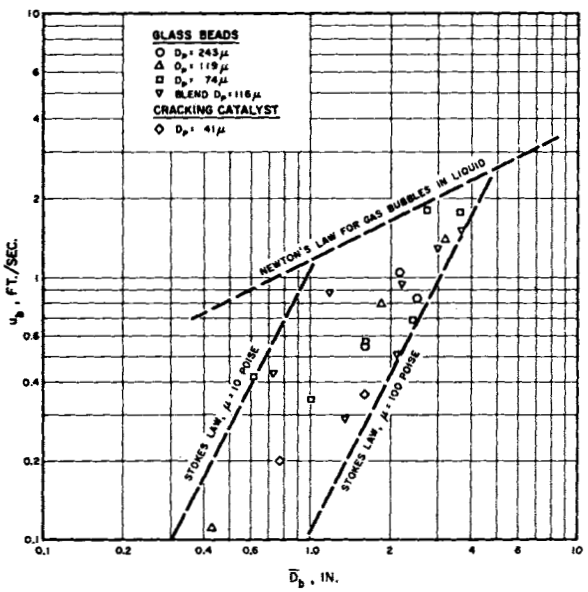

Fig. 15. Bubble velocity vs. bubble diameter.

TABLE 3. DENSE-PHASE DENSITY RELATIVE TO SETTLED-BED DENSITY

Material	Superficial air velocity, u_o, ft./sec.				
	0.05	0.08	0.2	0.7	2.0
Glass beads					
$D_p = 234\mu$	—	—	—	1.00	1.00
$D_p = 119\mu$	—	0.98	0.99	1.00	1.00
$D_p = 74\mu$	0.98	—	1.00	1.00	0.99
$D_p = 116\mu$ (Blend)	—	0.92	0.98	0.98	0.98
Cracking catalyst					
$D_p = 41\mu$	0.83	—	0.84	0.77	0.60

on the blend of glass beads indicated no clear-cut improvement from using a wide particle-size range. Also the smaller glass beads gave results not appreciably different from the larger glass beads when correlated on the basis of $u_0 - u_{omf}$. The only other important difference between the glass beads and cracking catalyst is the 45% lower bulk density of the catalyst. If bulk density is indeed a major factor in fluidized bed performance, it would not be possible to reproduce the behavior of the cracking catalyst with some size blend of the glass beads. On the other hand sufficient information is not available to state definitely that the smaller particle size and smoother particle-size distribution would not be factors. (Differences in particle shape and surface roughness are not believed to be important factors.)

Linear Bubble Velocity

In the case of gas bubbles rising through liquids the velocity of rise is a function of the bubble diameter. It is interesting to prepare a plot of this kind for the rise of bubbles in fluidized beds in order to compare the two cases. Such a plot is given in Figure 15. Lines are drawn for the terminal velocity of bubble rise through liquids according to Newton's law (motion governed by inertial forces only) and according to Stokes' law (motion governed by viscous forces only) for liquid viscosities of 10 and 100 poise (*6*).

Although showing appreciable scatter data points for the fluidized bed fall in a region bounded by the Newton's-Law line above and on the left and right by the two Stokes'-Law lines. If a single line were drawn to correlate the points, it would have a slope intermediate between those of the Newton's- and Stokes'-Law lines. It is interesting to note that Kramers' data on the shear stress-shear rate relation in fluidized beds (*8*) indicated viscosity values of the order of 40 poise. The plot therefore suggests that the rise of bubbles in fluidized beds is affected both by viscous and inertial forces and that the fluidized bed acts as if it possessed a viscosity in the range of 10 to 100 poise opposing bubble motion.

The plot also suggests the hypothesis that bubble velocity is an increasing function of bubble size. A bubble of a given size would therefore always have the same velocity regardless of its previous history, and its velocity would increase as its size grew. If this is true, it can be reasoned that bubble growth is partly due to the interception of small bubbles by larger bubbles. Small bubbles rising in the fluidized bed would be captured continually from below by larger bubbles rising faster than they do. The larger bubbles would continue to grow, so that near the top of a bed the small bubbles would have practically disappeared and only large bubbles would be left. This conclusion agrees with visual observation of large fluidized beds.

CONCLUSIONS

The gamma-ray absorption results indicate that bubbles grow chiefly from an influx of gas from the dense-phase mixture or from continuous capture of tiny bubbles too small to be detected in these experiments. The gas velocity in the dense phase ultimately drops to a value close to the minimum fluidizing velocity. Columns of limited cross section limit the horizontal growth of bubbles and may result in channeling. Good uniformity in cracking catalyst was characterized by a low rate of bubble growth and apparent expansion of the dense phase from the settled-bed density.

ACKNOWLEDGMENT

This work was carried out with the aid of a fellowship provided by the Ethyl Corporation.

NOTATION

a = concentration of dense phase, fraction by volume, 0
$\bar{a}$ = line average of a, 0
$\langle \bar{a} \rangle$ = time average of $\bar{a}$, 0
D = diameter, L
$\overline{D_b}$ = bubble diameter, mean of determinations along 3- and 6-in. path, L
f_b = bubble frequency as seen by scintillation detector, T^{-1}
f_b' = bubble frequency for the entire column cross section, T^{-1}
g_L = acceleration of gravity, LT^{-2}
g_c = conversion factor, $MLT^{-2}F^{-1}$
H = pressure head, L
I = intensity of radiation, counts per unit time
L = height of bed, L
p = pressure, FL^{-2}
S = cross section of column, L^2
T = time interval, T
u = linear velocity, LT^{-1}
W = weight of solids, F
x = horizontal dimension parallel to gamma-ray beam, L
$\overline{x}$ = mean apparent bubble thickness, L
X = length of gamma-ray path, L
y = horizontal dimension perpendicular to gamma-ray beam, L
Z = distance above distributor, L

Greek Letters

δ = duration of square bubble trace, T
ϵ = void fraction, 0
θ = time coordinate, T
μ = viscosity, $ML^{-1}T^{-1}$
ρ = density, ML^{-3}
ρ^* = density relative to settled bed, 0
σ = standard deviation
σ^2 = variance
ϕ = shape factor, 0

Subscripts

b = individual bubble
B = bubble phase
D = dense phase
f = fluidized bed
F = supporting fluid
m = measured
mf = minimum fluidization
N = noise
p = individual particle
s = settled bed
w = water
0 = superficial, taken over the entire bed cross section
γ = gamma-ray beam

Note: Dimensions of the variables are given in terms of M, mass; F, force; L, length; T, time; and 0, dimensionless.

LITERATURE CITED

1. Askins, J. W., G. P. Hinds, and F. Kunreuther, *Chem. Eng. Progr.*, **47**, 401 (1951).
2. Baerg, A., J. Klassen, and P. E. Gishler, *Can. J. Research*, **F28**, 287 (1950).
3. Baumgarten, P. K., Ph.D. dissertation, Univ. Del., Newark (1956).
4. Carman, P. C., *Trans. Inst. Chem. Eng. (London)*, **15**, 150, Part I (1937).
5. Grohse, E. W., *A.I.Ch.E. Journal*, **1**, 358 (1955).
6. Haberman, W. L., and R. K. Morton, Report 802, NS 715-102, The David W. Taylor Model Basin, Navy Department (1953).
7. Herdan, G., and M. L. Smith, "Small Particle Statistics," Elsevier Publishing Co., New York (1953).
8. Kramers, H. A., *Chem. Eng. Sci.*, **1**, 35 (1951).
9. Lewis, W. K., E. R. Gilliland, and W. C. Bauer, *Ind. Eng. Chem.*, **41**, 1104 (1949).
10. Matheson, G. L., W. A. Herbst, and P. H. Holt, *ibid.*, 1099 (1949).
11. Miller, C. O., and A. K. Logwinuk, *ibid.*, **43**, 1220 (1951).
12. Morse, R. D., and C. O. Ballou, *Chem. Eng. Progr.*, **47**, 199 (1951).
13. Schiff, L. I., and R. D. Evans, *Rev. Sci. Instr.*, **7**, 456, 62 (1936).
14. Sherwood, T. K., and C. E. Reed, "Applied Mathematics in Chemical Engineering," Chap. 9, McGraw-Hill, New York (1939).
15. Shuster, W. W., and Peter Kisliak, *Chem. Eng. Progr.*, **9**, 455 (1952).
16. Toomey, R. D., and H. F. Johnstone, *ibid.*, **48**, 220 (1952).
17. Untermyer, S., *Nucleonics*, **12**, No. 5, 35 (1954).
18. Wamsley, W. M., and L. N. Johanson, *Chem. Eng. Progr.*, **50**, 347 (1954)

Manuscript received July 18, 1957; revision received April 13, 1959; paper accepted April 15, 1959.